Delft University of Technology

An Interpretable Method for Operational Modal Analysis in Time-Frequency Representation and Its Applications to Railway Sleepers

Zeng, Yuanchen; Shen, Chen; Núñez, Alfredo; Dollevoet, Rolf; Zhang, Weihua; Li, Zili

Citation (APA)

Important note
To cite this publication, please use the final published version (if applicable).
Please check the document version above.

WILEY | Hindawi

Research Article

An Interpretable Method for Operational Modal Analysis in Time-Frequency Representation and Its Applications to Railway Sleepers

Yuanchen Zeng ,[1] **Chen Shen** ,[1] **Alfredo Núñez** ,[1] **Rolf Dollevoet**,[1,2] **Weihua Zhang**,[3] **and Zili Li** [1]

[1]*Section of Railway Engineering, Faculty of Civil Engineering and Geosciences, Delft University of Technology, Stevinweg 1, Delft, Netherlands*
[2]*ProRail B.V., Moreelse Park 3, Utrecht, Netherlands*
[3]*State Key Laboratory of Rail Transit Vehicle System, Southwest Jiaotong University, No. 111, North 1st Section of 2nd Ring Road, Chengdu, China*

Correspondence should be addressed to Zili Li; z.li@tudelft.nl

Operational modal analysis (OMA) enables the identification of modal characteristics under operational loads and conditions. Traditional frequency-domain methods cannot directly capture modal changes over time, while existing time-frequency representations are not sufficiently interpretable due to spurious modes and implicit parameter design. This paper develops a new OMA method in time-frequency representation based on frequency-domain decomposition (FDD). Short-time FDD and a convolution-based strategy are proposed to obtain singular values and local mode shape similarity, respectively, which are further fused into mode indicators by a fuzzy-based strategy mimicking the modal assurance criterion. The method provides not only a global view of the modal characteristics over time and frequency but also estimates of the modal parameters. It is applicable to strongly nonstationary responses under time-varying loads and conditions. All the parameters explicitly affect the time-frequency representation, and the interpretability is enhanced by including physical information from the user's prior knowledge in selecting parameters and peak bands. The proposed method is validated based on a study of railway sleepers under train passage. The rigid-body motions and bending modes are identified at frequencies up to 6,500 Hz in laboratory tests and 4,500 Hz in field tests at speeds up to 200 km/h. The identified natural frequencies and mode shapes agree with experimental modal analysis (EMA). The proposed method outperforms EMA in terms of broad frequency range and low measurement cost and can be potentially applied to structural health monitoring under operational conditions.

1. Introduction

Modal analysis is widely used in structural dynamics and structural health monitoring (SHM). In many cases of experimental modal analysis (EMA), it is difficult or expensive to manually excite a structure with a hammer or shaker [1] or to analyze changes in modal properties under varying loading conditions. Operational modal analysis (OMA) enables modal characteristics to be identified solely based on the response of a structure under operational loads and conditions. It does not require manual generation and sensing of excitations and is becoming increasingly popular in SHM.

OMA methods are generally classified into time-domain methods and frequency-domain methods. Time-domain methods are based on the analysis of time histories or correlation functions, e.g., natural excitation techniques, autoregressive moving average, stochastic subspace identification, blind source separation, and the Bayesian time-domain approach [2–4]. They are usually computationally

demanding and require proper selection of model order and the exclusion of spurious modes due to numerical computation [1, 2]. Frequency-domain methods are based on the Fourier spectrum or power spectral density (PSD), which are naturally more interpretable. The most basic frequency-domain method is the peak-picking method [1, 2], which considers one mode at a time. Least square frequency methods [5, 6] identify multiple modes together by iteratively estimating a parameterized spectrum. Furthermore, Bayes' theorem is incorporated to infer probability distributions of modal parameters [7], such as the spectral density approach [8], Fourier transform approach [9], Markov chain Monte Carlo approach [10], and expectation-maximization approach [11]. These Bayesian methods provide a rigorous formulation that makes full use of measurement data, but they face many challenges in solving ill-conditioned problems and estimating closely spaced modes [12].

Frequency-domain decomposition (FDD) is an extension of the peak-picking method, which can identify closely spaced modes and does not require numerical iterations [2]. The method was first used for modal analysis in [13] and then systematized to identify natural frequencies and mode shapes under broadband excitations in [14]. Since then, it has been applied to the SHM of many engineering structures [15–19]. Meanwhile, many variants of the FDD method have been proposed in the literature. The estimation of damping ratios is achieved by converting the PSD back to the time domain (known as enhanced FDD) [20, 21] or by fitting the PSD in the narrow frequency band of a mode [22, 23]. The FDD method is further adapted for nonstationary responses or heavily damped structures by jointly using two PSD estimates and detrending the correlation function [24, 25]. Moreover, model errors and measurement noise are incorporated into the analysis by estimating the PSD matrix via maximum likelihood [26].

The FDD-based methods can produce a spectrum describing the dominance of modes in frequency but cannot directly capture the change of modal characteristics over time. To address this issue, a time-frequency representation is needed. Time-frequency methods based on blind source separation were developed [27, 28], but they may produce spurious modes, and the numerical accuracy is sensitive to the number of sensors. As a popular time-frequency analysis method, continuous wavelet transform (CWT) was combined with ridge extraction in [29–32], but the performance of ridge extraction is sensitive to noise. Furthermore, CWT was combined with singular value decomposition, but proper selection of the mother wavelet and its parameters can be tricky because they are not directly related to structural dynamics, and a nonstationary signal over a long time horizon still needs to be split into segments [33, 34]. Thus, spurious modes and implicit parameter design reduce the physical interpretability of OMA. To the best of our knowledge, no existing method can produce a time-

frequency representation indicating both the dominance of structural modes and the correlation of their mode shapes.

This paper develops a new OMA method suitable for strongly nonstationary responses by extending the FDD method to a time-frequency representation. A study of railway sleepers under train passage is used to showcase the proposed method. EMA, especially hammer tests, has been widely applied in the modal analysis and SHM of railway tracks [35–37], whereas the application of OMA is rare [38]. Furthermore, the characteristics of the train-induced load on a sleeper vary considerably as the train approaches, passes, and leaves, which further affect the stiffness and damping of track components [39–41]. As a result, the sleeper vibration in response to train passage is significantly nonstationary. In addition, the damping effect from rail pads and ballast makes modal identification more challenging.

The main contributions of this paper are summarized as follows. First, the proposed method incorporates the interpretability of FDD into time-frequency representation. It can produce spectrograms indicating the dominance of structural modes and also the local similarity of their mode shapes. All the parameters explicitly affect the time-frequency representation and can be selected based on the physical information from the user's prior knowledge. Second, the proposed method provides not only a global view of the modal characteristics over time and frequency but also estimates of the modal parameters. It is applicable to strongly nonstationary responses under time-varying loads and conditions and is also robust to the length of signals. Third, the proposed method is demonstrated to identify the rigid-body motions and bending modes of railway sleepers in different train passage phases and at different speeds. This paper also showcases its capability to distinguish closely spaced modes using numerical simulation.

The remainder of this paper is organized as follows. In Section 2, the fundamentals of FDD are briefly introduced. In Section 3, the new OMA method and the corresponding parameter selection strategy are proposed. In Section 4, the proposed method is validated through theoretical analysis and laboratory experiments. In Section 5, the proposed method is applied to field tests and compared with EMA. Finally, some discussions are presented in Section 6, and the conclusions are summarized in Section 7.

2. Fundamentals of FDD

Structural responses are usually measured by accelerometers at a sampling frequency f_s. Estimating the PSD matrix of the response is the first step in FDD, for which Welch modified periodogram method [42] is widely used owing to its computational efficiency [2]. First, the measured response is divided into n_c overlapped (overlap ratio α_b) segments of equal length n_b, and a window function tapers each segment to reduce the leakage effect. The recommended overlap ratio

α_b and window function are 0.5 and Hanning window, respectively [42]. Then, the modified periodogram $\mathbf{I}_k(f_n)$ is calculated for each windowed segment based on the fast Fourier transform (FFT), where f_n is the n-th discrete frequency as follows [42]:

$$f_n = \frac{n f_s}{n_b} \quad n = 0, \cdots, \frac{(n_b - 1)}{2}, \frac{n_b}{2}. \tag{1}$$

Next, the PSD matrix at each frequency f_n is estimated by averaging the periodograms over all n_c segments as follows [42]:

$$\widehat{\mathbf{S}}_{yy}(f_n) = \frac{1}{n_c} \sum_{k=1}^{n_c} \mathbf{I}_k(f_n). \tag{2}$$

Once $\widehat{\mathbf{S}}_{yy}(f_n)$ is obtained, singular value decomposition (SVD) is applied as follows [2]:

$$\widehat{\mathbf{S}}_{yy}(f_n) = \mathbf{U}(f_n)\mathbf{V}(f_n)\mathbf{U}(f_n)^H, \tag{3}$$

where $\mathbf{V}(f_n)$ is a diagonal matrix with singular values arranged in descending order and $\mathbf{U}(f_n)$ is a unitary matrix containing the singular vectors corresponding to the singular values. At each frequency f_n, a singular value in $\mathbf{V}(f_n)$ indicates the contribution of the corresponding singular vector in $\mathbf{U}(f_n)$, just as a modal response indicates the contribution of the corresponding mode shape based on the modal expansion of the structural response [2].

Mathematically, the number of segments n_c in PSD estimation determines the number of nonzero singular values in $\mathbf{V}(f_n)$ at each frequency [14], and multiple nonzero singular values allow for the identification of closely spaced modes. All nonzero singular values can be plotted in a spectrum, where a resonance peak indicates the possible existence of a mode at the corresponding frequency. To further confirm such a mode, the singular vector of the peak is usually compared with other singular vectors at its adjacent frequencies. A popular scheme to quantify the similarity between two vectors is the modal assurance criterion (MAC) [2], denoted as $MAC(p, q)$, which is equal to 0 (or 1) when the two vectors, p and q, are orthogonal (or proportional). If the singular vectors in the vicinity of a peak are of high similarity (MAC greater than a threshold), they are identified as belonging to the same dominant mode [2, 24].

Once a mode is confirmed, its modal parameters can be estimated following the strategy of enhanced FDD [20, 21]. First, an auto PSD function is created using the identified singular values at the corresponding frequencies, representing an equivalent single degree of freedom system. Then, an inverse FFT is applied to the auto PSD to obtain an autocorrelation function in the time domain. The zero crossings of the autocorrelation function can give an estimate of the damped natural frequency, while the extremes are used to estimate the logarithmic decrement δ through linear regression. Further, the damping ratio is calculated as follows [20, 21]:

$$\xi = \frac{\delta}{\sqrt{\delta^2 + 4\pi^2}}. \tag{4}$$

Finally, a real-valued mode shape vector can be obtained from each of the identified singular vectors. A simple approach [2] is to normalize the complex singular vector by the maximum absolute value of its components and then rotate each component to 0°(or 180°) if its phase lies in the first or fourth (or the second or third) quadrant. A mode shape vector can be displayed with respect to sensor positions in a static plot. It is noteworthy that the problem of spatial aliasing can occur when the number of sensors is insufficient. In this case, the identified mode shape should be interpreted carefully.

In general, the validity of FDD is based on the assumptions of white noise excitations, low structural damping ratios, and orthogonal mode shapes for closely spaced modes [24]. If these assumptions are not fully satisfied or if measurement noise is present, the identification result is an approximation to real modal characteristics [24, 43].

3. Time-Frequency Representation of OMA (TFOMA)

This paper develops a new OMA method, named, TFOMA, by extending the FDD method to a time-frequency representation. Figure 1 shows its framework. First, short-time FDD and a convolution-based strategy are proposed to obtain singular values and local mode shape similarity, respectively. Then, they are fused into mode indicators by a fuzzy-based strategy, and modal parameters are further estimated. Sections 3.1–3.3 will introduce these main steps, and Section 3.4 will discuss the parameter selection strategy.

3.1. Short-Time FDD (STFDD). In FDD, the Fourier transform is used to average the frequency information over the entire signal time, which is theoretically applicable to stationary processes. The short-time Fourier transform [44] is a modified version of the Fourier transform for strongly nonstationary signals. We apply a similar strategy to FDD as follows and name it short-time FDD (STFDD):

$$\mathbf{STFDD}\{\mathbf{y}(s)\}(t, f) = \mathbf{FDD}\{\mathbf{y}(s)r(s - t)\}(f), \tag{5}$$

where $\mathbf{y}(s)$ is the vector of synchronized measurement from multiple sensors at sampling time s and $r(s - t)$ represents a rectangular window centered at t.

As illustrated in Figure 2, $\mathbf{y}(s)$ is broken into segments of equal length with an overlap ratio α_s, and the procedures of PSD estimation and SVD are applied to each segment, producing a series of singular value matrices $\mathbf{V}(t, f)$ and singular vector matrices $\mathbf{U}(t, f)$. The k-th diagonal term in $\mathbf{V}(t, f)$ is denoted as $v_k(t, f)$, and the k-th singular vector in $\mathbf{U}(t, f)$ is denoted as $\mathbf{u}_k(t, f)$. At the k-th level, a singular value spectrogram can be obtained by plotting $v_k(t, f)$ over time and frequency with color mapping. According to Section 2, the number of effective spectrograms is equal to the number of nonzero singular values, which is further equal to n_c used
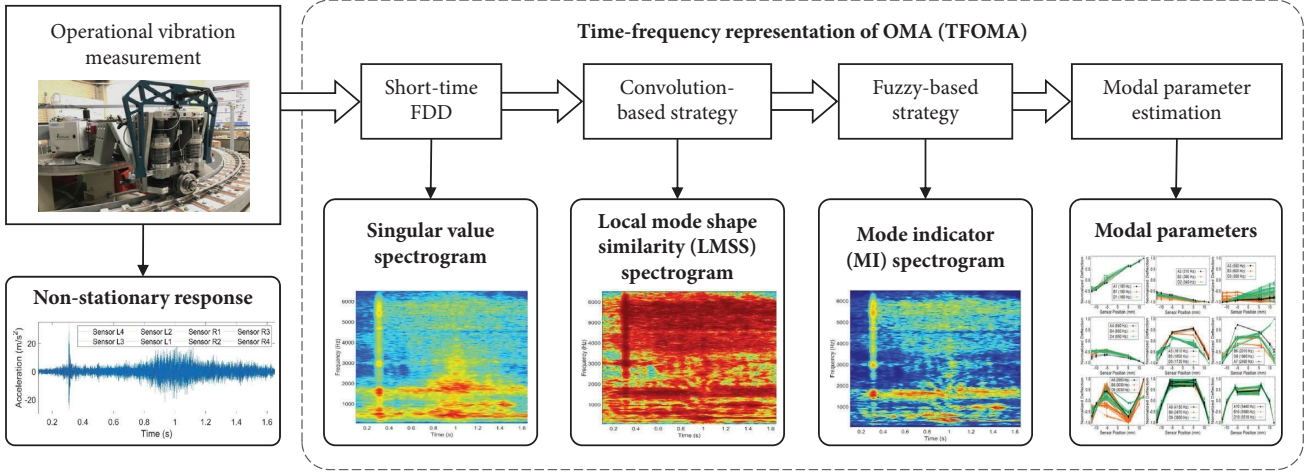
FIGURE 1: Framework of TFOMA.

in PSD estimation. It is noteworthy that STFDD also holds the drawbacks of STFT, the most significant of which is the trade-off between time and frequency resolutions (discussed in Section 3.4).

3.2. Local Mode Shape Similarity (LMSS). A peak in a singular value spectrogram indicates the possible existence of a structural mode. According to MAC, a mode is effectively dominant when the singular vector of the peak has a high similarity to the singular vectors in its vicinity. To enable comparisons in both time and frequency dimensions, we propose a convolution-based strategy to quantify the local similarity of singular vectors. In a two-dimensional representation, e.g., an image, convolution works by applying a kernel to each location and evaluating the central element based on all elements in the kernel [45, 46]. In the time-frequency representation, we adapt it to compute the following scalar, named, local mode shape similarity (LMSS):

$$l_k(t, f) = \sum_{\mathrm{d}t=-a}^{a} \sum_{\mathrm{d}f=-b}^{b} \omega(\mathrm{d}t, \mathrm{d}f) \cdot MAC\left(\mathbf{u}_k(t, f), \mathbf{u}_k(t + \mathrm{d}t \cdot \Delta t, f + \mathrm{d}f \cdot \Delta f)\right), \tag{6}$$

where a and b are the half kernel sizes (number of elements) in time and frequency, respectively, Δt and Δf are the time and frequency resolutions, respectively, and $\omega(\mathrm{d}t, \mathrm{d}f)$ represents the weight assigned for each element in the kernel.

LMSS is a weighted sum of *MAC* values between the central element and all other elements in a kernel. In this paper, a separable kernel with Gaussian functions [46, 47] is used, and the weights are determined as follows:

$$\omega(\mathrm{d}t, \mathrm{d}f) = \begin{cases} 0, & \text{if } \mathrm{d}t = 0 \text{ and } \mathrm{d}f = 0, \\ \dfrac{\omega_0(\mathrm{d}t, \mathrm{d}f)}{\sum_{\mathrm{d}t'=-a}^{a} \sum_{\mathrm{d}f'=-b}^{b} \omega_0\left(\mathrm{d}t', \mathrm{d}f'\right) - \omega_0(0, 0)}, & \text{otherwise,} \end{cases} \tag{7}$$

where the weight of the central element is zero and $\omega_0(\mathrm{d}t, \mathrm{d}f)$ is the unnormalized weight calculated based on the following Gaussian functions:

$$\omega_0(\mathrm{d}t, \mathrm{d}f) = \exp\left(-\frac{\mathrm{d}t^2}{2\sigma_t^2}\right) \cdot \exp\left(-\frac{\mathrm{d}f^2}{2\sigma_f^2}\right) \cdot \exp\left(-\frac{\mathrm{d}v_{(t,f)}(\mathrm{d}t, \mathrm{d}f)^2}{2\sigma_v^2}\right), \tag{8}$$
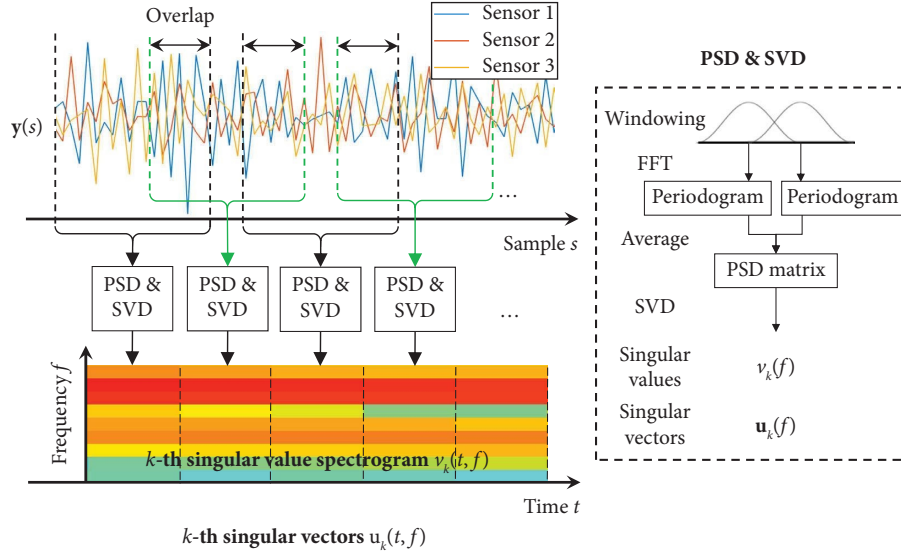
Figure 2: Short-time FDD and singular value spectrogram.

where $dv_{(t, f)}(dt, df)$ denotes the logarithmic difference in singular values with respect to the central element, as calculated as follows:

$$dv_{(t,f)}(dt, df) = \log[v_k(t + dt \cdot \Delta t, f + df \cdot \Delta f)] - \log[v_k(t, f)]. \tag{9}$$

Furthermore, σ_t, σ_f, and σ_v are standard deviations characterizing the decay rates of the weight as dt, df, and dv increase, respectively. We recommend determining them as follows:

$$\sigma_t = \frac{a+1}{3} \quad \sigma_f = \frac{b+1}{3} \quad \sigma_{v_{(t,f)}} = \sqrt{\frac{1}{(2a+1) \cdot (2b+1) - 1} \sum_{dt=-a}^{a} \sum_{df=-b}^{b} \left[dv_{(t,f)}(dt, df)\right]^2}. \tag{10}$$

Equations (8)–(10) reflect that, from the kernel center to the kernel boundary, the weight decreases from one to zero as dt or df increases, according to the three-sigma rule. This property allows comparisons to be made in a localized manner with smooth transitions at kernel boundaries. Additionally, the weight is lower when an element's singular value deviates more from the center's. This property enhances the adaptability of LMSS to structural modes with different bandwidths since the weight decays faster in the case of a sharper resonance peak and vice versa. Meanwhile, it allows LMSS to better capture the shift in resonance frequency over time.

Figure 3 illustrates the calculation process of LMSS at the k-th level. An LMSS spectrogram can be obtained by plotting $l_k(t, f)$ over time and frequency with color mapping. The value of each point indicates the similarity of mode shapes between that point and its vicinity, and a peak region indicates a high local similarity at that time and frequency, which can help to confirm the dominance of a mode.

3.3. Mode Indicator (MI).

After obtaining the singular value spectrogram and the LMSS spectrogram, structural modes can be identified from regions with both large singular values
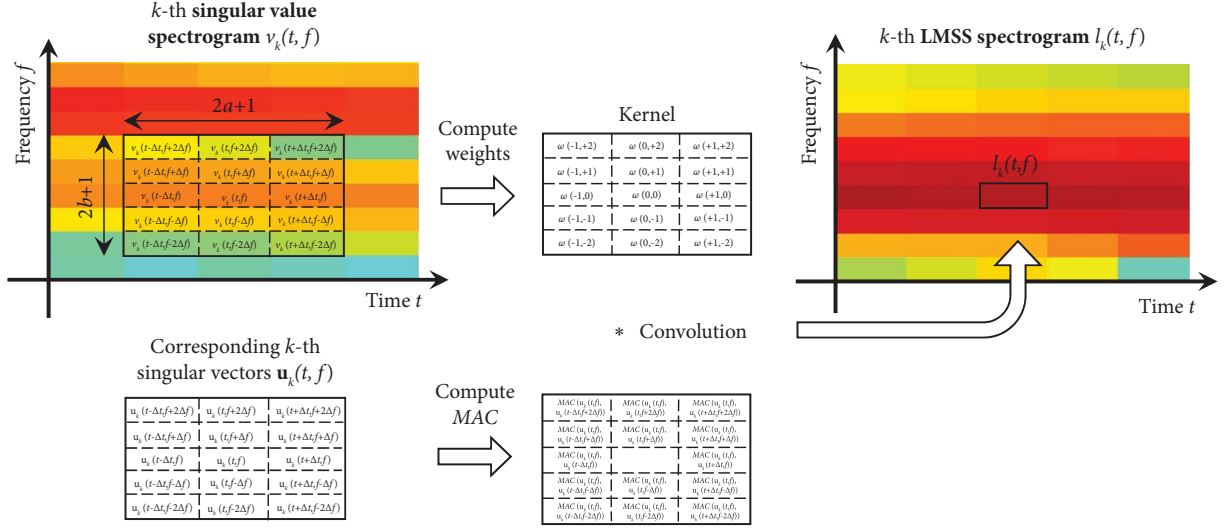
FIGURE 3: Local mode shape similarity and its spectrogram.

and large LMSS. In this paper, a fuzzy-based fusion strategy is proposed to fuse $v_k(t, f)$ and $l_k(t, f)$ at each time and frequency into a mode indicator (MI), denoted as $MI_k(t, f)$. Fuzzy set theory quantifies the membership of an element in a set through a membership function [48], which is usually used to handle vague information, e.g., fusing multiple images [49–51]. It is suitable for computing MI because there is no precise relationship to determine the existence of modes based on $v_k(t, f)$ and $l_k(t, f)$ but rather a soft and flexible thresholding strategy according to MAC.

First, all $v_k(t, f)$ and $l_k(t, f)$ are normalized as follows:

$$
\begin{cases}
v_k'(t, f_n) = \dfrac{\log\left(v_k(t, f)\right) - \min\left(\log v_k(t, f)\right)}{\max\left(\log\left(v_k(t, f)\right)\right) - \min\left(\log\left(v_k(t, f)\right)\right)}, \\[3mm]
l_k'(t, f) = \dfrac{l_k(t, f) - \min\left(l_k(t, f)\right)}{\max\left(l_k(t, f)\right) - \min\left(l_k(t, f)\right)}.
\end{cases}
\tag{11}
$$

Then, we use the following membership function to compute the MI:

$$
MI_k(t, f) = \left[v_k'(t, f)\right]^{\lambda_v} \cdot \left[l_k'(t, f)\right]^{\lambda_l}, \tag{12}
$$

where λ_v and λ_l are the contribution exponents of $v'_k(t, f)$ and $l'_k(t, f)$, respectively.

Figure 4 illustrates the calculation process of MI, in which the membership function with $\lambda_v = 1$ and $\lambda_l = 3$ is shown as an example. It can be seen that $MI_k(t, f)$ approaches 0 when $v_k'(t, f)$ or $l_k'(t, f)$ is small and tends to 1 as $v_k'(t, f)$ and $l_k'(t, f)$ increase. Meanwhile, $l_k'(t, f)$ is more dominant than $v_k'(t, f)$ owing to the selection of λ_v and λ_l. As a consequence, when $l_k'(t, f)$ is less than 0.45, $MI_k(t, f)$ is lower than 0.1 even if $v_k'(t, f)$ is large. The selection of λ_v and λ_l enables the proposed fuzzy-based strategy to mimic a thresholding strategy of MAC and provide a soft and interpretable fusion between $v_k(t, f)$ and $l_k(t, f)$.

As shown in Figure 4, the computed MIs at the k-th level $MI_k(t, f)$ are plotted as an MI spectrogram with peak regions indicating the presence of structural modes. Then, a frequency band that peaks continuously over time at physically meaningful frequencies can be selected for each mode. To further estimate the modal parameters of a mode, the singular values in its frequency band with MIs greater than a threshold are selected to create auto PSD functions, which can then be used to estimate the natural frequency and damping ratio at each time instant (see Section 2). Meanwhile, the singular vectors corresponding to the selected singular values can be converted into mode shape vectors (see Section 2). Therefore, the proposed method provides not only a global view of the modal characteristics over time and frequency but also estimates of the modal parameters.

3.4. Parameter Selection Strategy. The time-frequency representation of the proposed method depends on the selection of its parameters. Sufficient time and frequency resolutions are necessary for clear visualization of modal characteristics and accurate estimation of the modal parameters. The frequency resolution Δf and the time resolution Δt are determined as follows:

$$
\Delta f = \frac{f_s}{n_b} \quad \Delta t = \frac{n_b(1 - \alpha_s)\left[n_c(1 - \alpha_b) + \alpha_b\right]}{f_s}. \tag{13}
$$

We propose the following strategy to select all the parameters of the TFOMA method.

Step 1. Select the number of segments n_c in PSD estimation. As mentioned in Sections 2 and 3.1, n_c determines the number of nonzero singular values. For structures with separated modes, n_c can be set to 1, whereas in cases of closely spaced modes, n_c should be greater than the maximum number of physical modes in each identified frequency band.
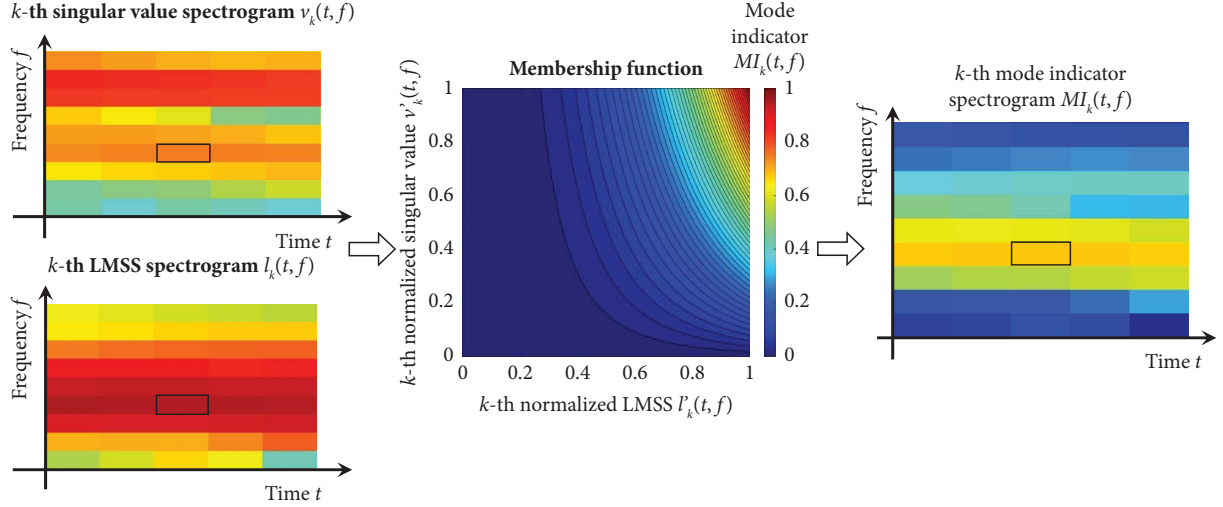
Figure 4: Membership function and mode indicator spectrogram.

Step 2. Select the segment length n_b in PSD estimation and the overlap ratio α_s in STFDD. According to (13), they directly affect Δf and Δt: larger n_b leads to smaller Δf but larger Δt, and larger α_s leads to smaller Δt but higher computational costs. We recommend first selecting n_b to provide sufficient frequency resolution, e.g., at least five discrete frequencies in the frequency band of a mode. Then, α_s can be selected to provide sufficient time resolution, e.g., Δt to be shorter than the nonstationary behavior of the signal.

Step 3. Select the half kernel sizes a and b. Under defined Δt and Δf, the kernel lengths in time and frequency are $(2a + 1) \cdot \Delta t$ and $(2b + 1) \cdot \Delta f$, respectively. For comparisons in a localized manner, we recommend setting a and b as small integers, such as 3~10, to ensure that $(2a + 1) \cdot \Delta t$ and $(2b + 1) \cdot \Delta f$ are shorter than the duration and bandwidth of each mode, respectively.

Step 4. Select the contribution exponents λ_v and λ_l. As exemplified in Section 3.3, we recommend setting $\lambda_l > \lambda_v = 1$ to mimic a thresholding strategy of MAC. The larger λ_l is, the greater the influence of LMSS on MI, i.e., a higher LMSS is required to reach a certain level of MI.

All parameters in the TFOMA method explicitly affect the time-frequency representation. They can be selected and tuned according to the user's prior knowledge of the structural dynamics and goals of analyses.

4. Validation via Laboratory Tests

4.1. TFOMA of an **In Situ** *Sleeper.* We validate the proposed TFOMA method on the V-Track test rig at TU Delft [52], which resembles train-track interaction. As shown in Figure 5, the track consists of rails, sleepers, foundations, and fastening systems. A beam is driven by a motor to rotate around the central axis of the test rig, and the wheel at the end of the beam rolls along the track. The wheel is vertically loaded by a suspension system, and the static wheel load is

1,300 N in our measurement. There are four rail joints in the test rig. When the wheel passes over these joints, significant impacts occur.

We instrument one sleeper with eight accelerometers (PCB 356B21) on its top surface. The vertical accelerations are measured at the sampling frequency of $f_s = 102,400$ Hz. The running speed of the wheel is 8 km/h. Figure 6(a) plots the measured sleeper accelerations with four phases distinguished, which shows significant nonstationarity. Phase A is caused by the passage over a joint that is several sleepers away from the instrumented sleeper. It is similar to the response of a hammer test. Phases B~D belong to the response caused by the wheel passage, divided into prepassage, underpassage, and postpassage phases.

We apply the TFOMA method to the measured data with the parameters listed in Table 1. The spectrograms of singular value, LMSS, and MI are shown in Figure 6 at frequencies up to 6,500 Hz. As shown in Figures 6(c) and 6(d), most of the large singular values are located below 2,000 Hz, while large LMSS is present throughout the frequency range. By fusing the singular values with the LMSS, we obtain the MI spectrogram in Figure 6(b), which shows peak regions with sharper edges than those in Figures 6(c) and 6(d), making them easier to be picked up.

In the MI spectrogram, the impact response in Phase A produces a vertical ridge, along which the MI peaks at some frequencies. In Phases B and D, a number of peak bands can be observed, which continuously dominate at frequencies close to the peaks in Phase A. The peaks in Phase C are less clear as they belong to the forced response phase. We select ten peak bands in Phases A, B, and D, as labeled in Figure 6(b), where the label height represents the bandwidth. At low (or high) frequencies, the density of peak bands is high (or low), and their bandwidths are narrow (or wide). In each selected band, we use points with MI greater than 0.4 for further parameter estimation, and the identified mode shapes and average natural frequencies are shown in Figure 7. Most identification results are consistent between
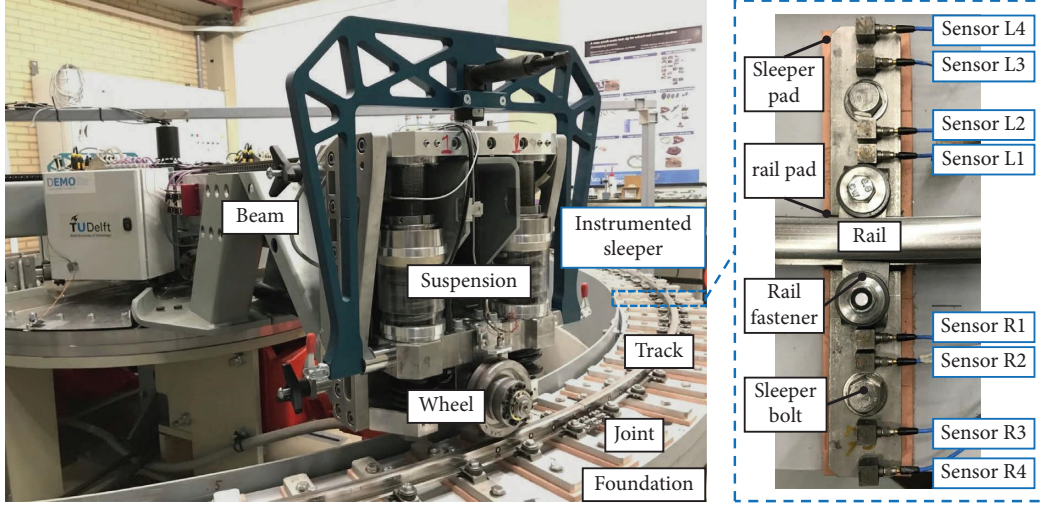
FIGURE 5: The V-Track test rig and the instrumented sleeper.

Phases A, B, and D, though the passage response suffers more nonstationarity and noise.

4.2. EMA and Theoretical Analysis of a Free Sleeper. To verify the above identification results, we perform hammer tests on a free sleeper of the same type on an elastic foundation. Since the sleeper is free of rail fasteners, it is instrumented with more distributed accelerometers (PCB 356B21), as shown in Figure 8(a). We use a small hammer (Brüel & Kjær 8206-003) to generate the impact at each of the four locations.

To reduce the effect of leakage and noise, the measured response from each sensor is tapered by an exponential window, and the measured force is tapered by the same exponential window and also a force window [53]. Then, for the i-th sensor ($i = 1, \ldots, 9$) in response to the impact at the j-th location ($j = 1, \ldots, 4$), we compute the cross-spectrum between the acceleration and the force $S_{a_i p_j}(f)$ and the auto-spectrum of the force $S_{p_j p_j}(f)$ through the Fourier transform. Furthermore, the frequency response function (FRF), more specifically the receptance function, is calculated as follows [54]:

$$H_{ij}(f) = \frac{S_{a_i p_j}(f)}{S_{p_j p_j}(f)(2\pi f)^2}. \qquad (14)$$

An FRF is a complex function of frequency that describes the response of a structure at the sensor position to excitation at the impact location. A resonance peak indicates the presence of a structural mode at the corresponding frequency. The mode shape vector can be obtained by combining the imaginary parts of the FRFs from different sensors as follows [54]:

$$\left[\operatorname{Im}\left(H_{1j}(f) \right), \ \operatorname{Im}\left(H_{2j}(f) \right), \ \cdots, \ \operatorname{Im}\left(H_{9j}(f) \right) \right]^{\mathrm{T}}. \qquad (15)$$

At each impact location, we repeat the test three times and average the FRFs as the final result. For example, Figure 8(b) plots the magnitude of the FRFs for all sensors in response to Impact 2. Four resonance peaks are identified from all FRFs at different impact locations, labeled as $P0 \sim P3$, and their mode shapes and average frequencies are shown in Figure 8(c).

Meanwhile, we calculate the theoretical mode shapes by simplifying the sleeper as a free-free beam. Based on its boundary conditions, the n-th order mode shape is given as follows [55]:

$$w_n(x) = \left[\sinh(k_n x) + \sin(k_n x) \right] + \frac{\sin(k_n L) - \sinh(k_n L)}{\cosh(k_n L) - \cos(k_n L)} \left[\cosh(k_n x) + \cos(k_n x) \right], \qquad (16)$$

where L is the beam length, x is the coordinate along the beam ($0 \le x \le L$), sinh and cosh are hyperbolic functions, and k_n is the n-th (numerical) solution of the following equation of k:

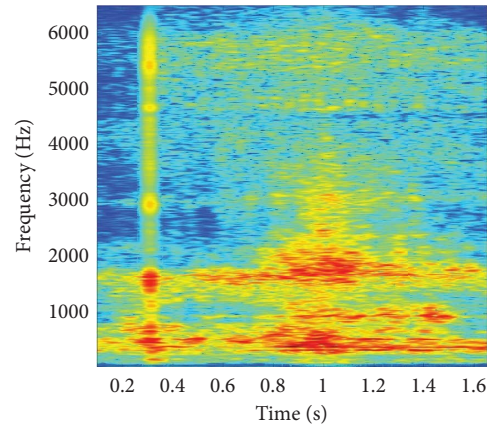$$\cosh(kL)\cos(kL) = 1. \qquad (17)$$

The mode shapes of a free-free beam with $L = 25$ cm are computed and plotted in Figure 8(c). Clearly, the mode shapes of $P1 \sim P3$ are in good agreement with the theoretical mode shapes of the first three bending modes, respectively, and $P0$ is the rigid-body motion of the sleeper.
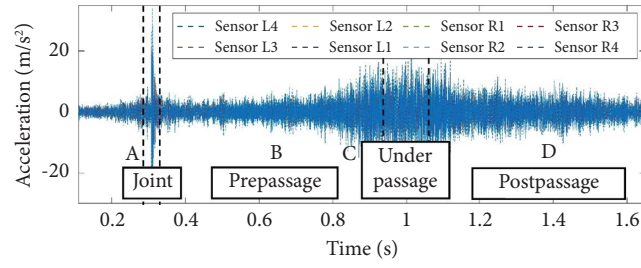
(a)
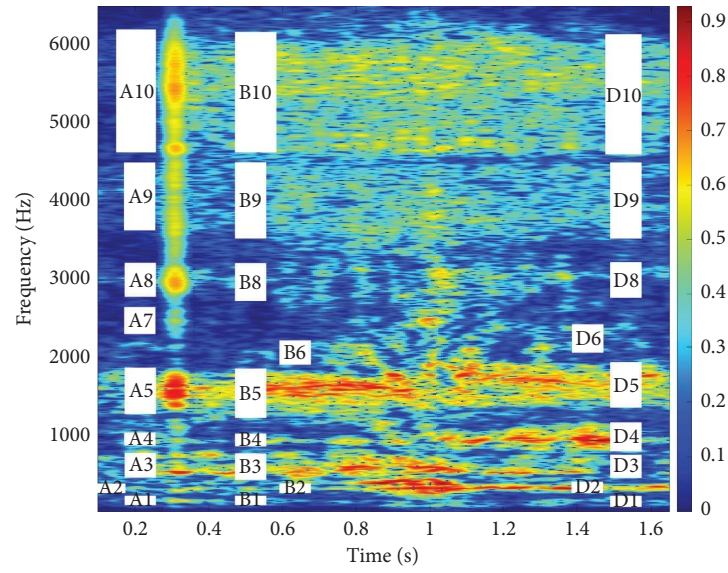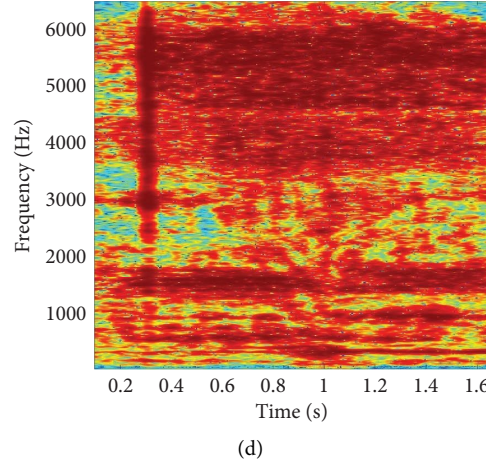

(b)

(c)

Figure 6: Continued.

(d)

FIGURE 6: TFOMA results of laboratory tests: (a) sleeper accelerations in the time domain; (b) MI spectrogram; (c) singular value spectrogram; (d) LMSS spectrogram.

4.3. EMA of the **In Situ** *Sleeper.* Hammer tests are also performed on the *in situ* sleeper in Section 4.1 using the same hammer. The locations of impacts and sensors are shown in Figure 9(a). We repeat the test five times at each location, which is more than that of the free sleeper due to lower repeatability. The average FRFs for the first two impact locations are shown in Figure 9(b) as examples. Seven resonance peaks are identified, labeled as Q1~Q7. The corresponding natural frequencies and mode shapes are shown in Figure 9(c).

Compared with the free sleeper, the *in situ* sleeper shows more resonance peaks below 2,000 Hz, and their mode shapes deviate for different impact locations. Q1~Q4 correspond to rigid-body motions but are not comparable to P0 due to different boundary conditions. Q5~Q7 correspond to P1~P3 (the first three bending modes), respectively. The results of Q5 and P1 show significant deviations. The frequencies of Q6 and P2 are consistent, while those of Q7 and P3 deviate slightly. Besides, the peaks of the *in situ* sleeper are smoother due to the damping effect. The above findings reflect the differences in modal characteristics due to different boundary conditions and also the influence of other track components.

4.4. Comparisons between TFOMA and EMA. By comparing the identification results of TFOMA and EMA for the same *in situ* sleeper, we find that:

(i) A1/B1/D1~A4/B4/D4 in TFOMA correspond to Q1~Q4 in EMA (the rigid-body motions). They have similar frequency bands, but the bounce motion is more dominant in TFOMA, while the roll motion is more dominant in EMA. This indicates that the rigid-body motions are sensitive to the characteristics of excitations.

(ii) A5/B5/D5 in TFOMA corresponds to Q5 in EMA (the 1st bending mode) with an MAC of 0.92/0.93/ 0.44. Among the first three bending modes, the 1st bending mode is the most dominant in both

TFOMA and EMA. The frequencies of TFOMA are lower than that of EMA, and A5/B5 provides a higher MAC than D5.

(iii) A8/B8/D8 in TFOMA corresponds to Q6 in EMA (the 2nd bending mode) with the MAC of 0.95/0.98/ 0.87. Their frequencies are consistent.

(iv) A10/B10/D10 in TFOMA corresponds to Q7 in EMA (the 3rd bending mode) with the MAC of 0.98/ 0.97/0.98. Their frequencies are consistent.

(v) B6/D6/A7 and A9/B9/D9 in TFOMA belong to extra modes related to other track components, e.g., rails.

In summary, TFOMA provides comparable identification results to EMA. The differences in the identified modal parameters reflect the influence of a moving train load on track dynamics. Among the three phases in TFOMA, the impact response and the prepassage phase outperform the postpassage phase in terms of mode shape consistency with EMA.

5. Application to Field Tests

5.1. TFOMA of an **In Situ** *Sleeper.* We test the proposed method using sleeper vibrations measured at the Faurei Railway Test Center in Romania. The track consists of UIC60 E1 rails, Vossloh W14 fastening systems, and B70-W60 prestressed concrete sleepers. As shown in Figure 10, four accelerometers (Brüel & Kjær 4514-004) are mounted on a sleeper. A train passes over the instrumented sleeper at three different speeds −15 km/h, 80 km/h, and 200 km/h. The vertical accelerations are recorded at a sampling frequency of 25,600 Hz. We find that Sensor L2 was not functional, most likely due to a loose installation, so we use the data from the other three functional sensors for analysis.

The TFOMA method is applied to the measured data with the parameters listed in Table 2. According to Section 4, only the prepassage phases are studied, while different lengths of signals are used due to the difference in speeds. The raw data and the corresponding MI spectrograms up to

TABLE 1: Selected parameters for laboratory tests.

Number of segment n_c	Segment length n_b	Overlap ratio in PSD estimation α_b	Overlap ratio in STFDD α_s	Half kernel size in time a
1	10240 (0.1 s)	0.5	0.95	10
Half kernel size in frequency b	Contribution exponent of singular value λ_v	Contribution exponent of LMSS λ_l	Time resolution Δt	Frequency resolution Δf
5	1	3	5 ms	10 Hz
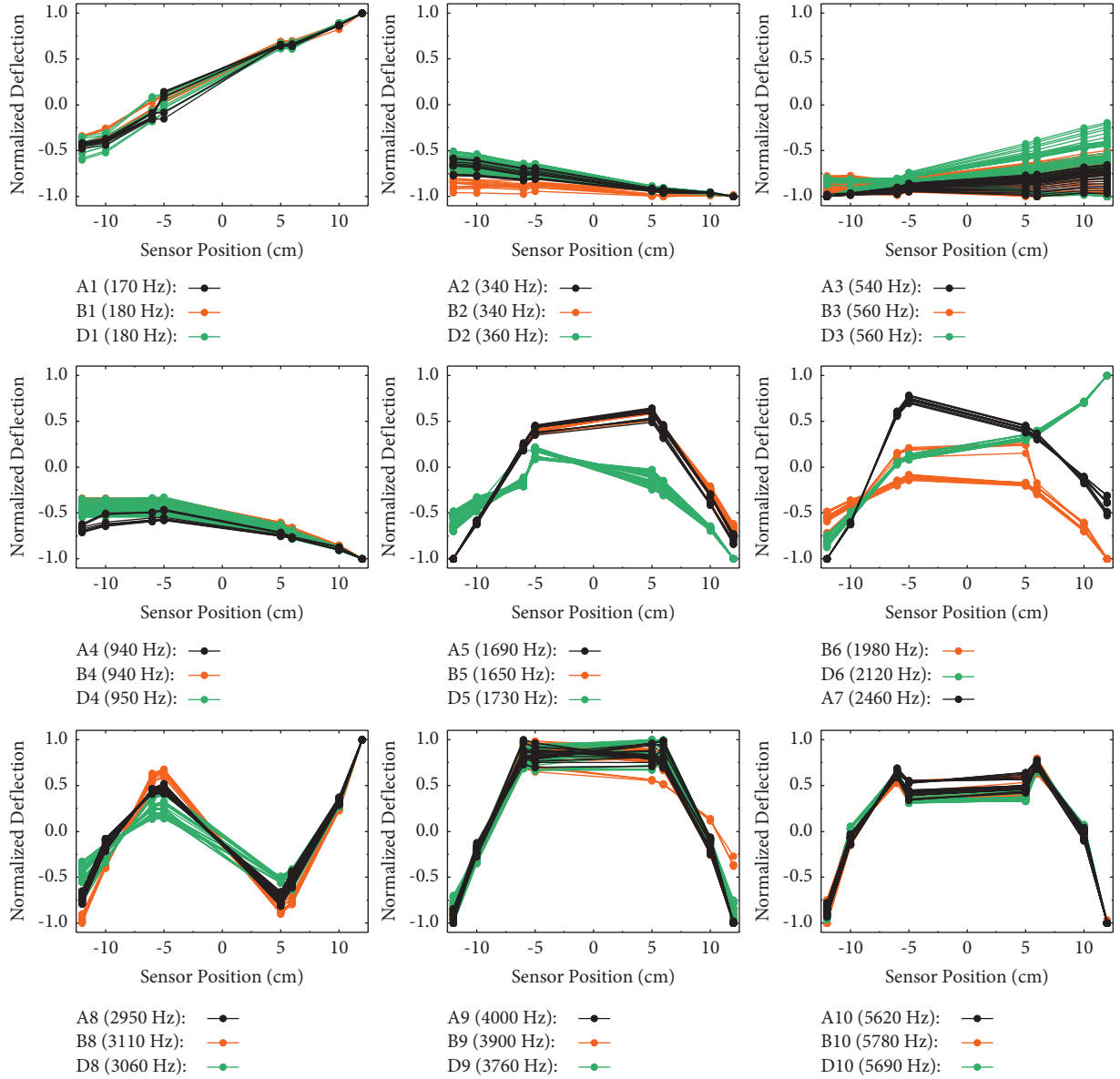
Figure 7: Modal identification results of laboratory tests.

4,500 Hz are shown in Figure 11. Generally, the patterns of MI are similar at different speeds. Some peak bands are wide in frequency, whereas others are narrow. The low-frequency bands are more pronounced at low speeds, especially when the train is close to the sleeper, whereas the high-frequency bands are more pronounced at high speeds and continuously dominant even when the train is still far away from the sleeper. In addition, some peak bands are not horizontal, i.e., their frequencies change as the train approaches.

We select fourteen peak bands at each speed, labeled as O1~O14. The first four columns of Table 3 present the characteristics of each peak band and also the average natural frequencies and mode shapes. In each plot, the identified mode shapes at a certain speed are plotted in a light color, and their average is plotted in a dark color. In general, the identified frequencies and mode shapes are similar at different speeds while varying slightly due to the

influence of train speed and noise. More discussion is provided in Section 5.3.

5.2. EMA of the In Situ Sleeper.

For comparison, we perform hammer tests with the same setup in Figure 10. All the four sensors were functional in the tests. We generate impacts at five locations using a big hammer (PCB 086D50) and a small hammer (PCB 086D05). At each location, we repeat the test five times with each hammer. Considering their different excitation frequencies [56], the results of the big and small hammers are used for analyses below 2,000 Hz and above 500 Hz, respectively. The average FRFs are plotted in Figure 12, and eleven resonance peaks are identified, labeled as E1~E11. Compared to the sleeper on the test rig, the natural frequencies of the real sleeper are much lower due to its size and material. Most of the resonance peaks, especially at high

(a)

(b)

(c)
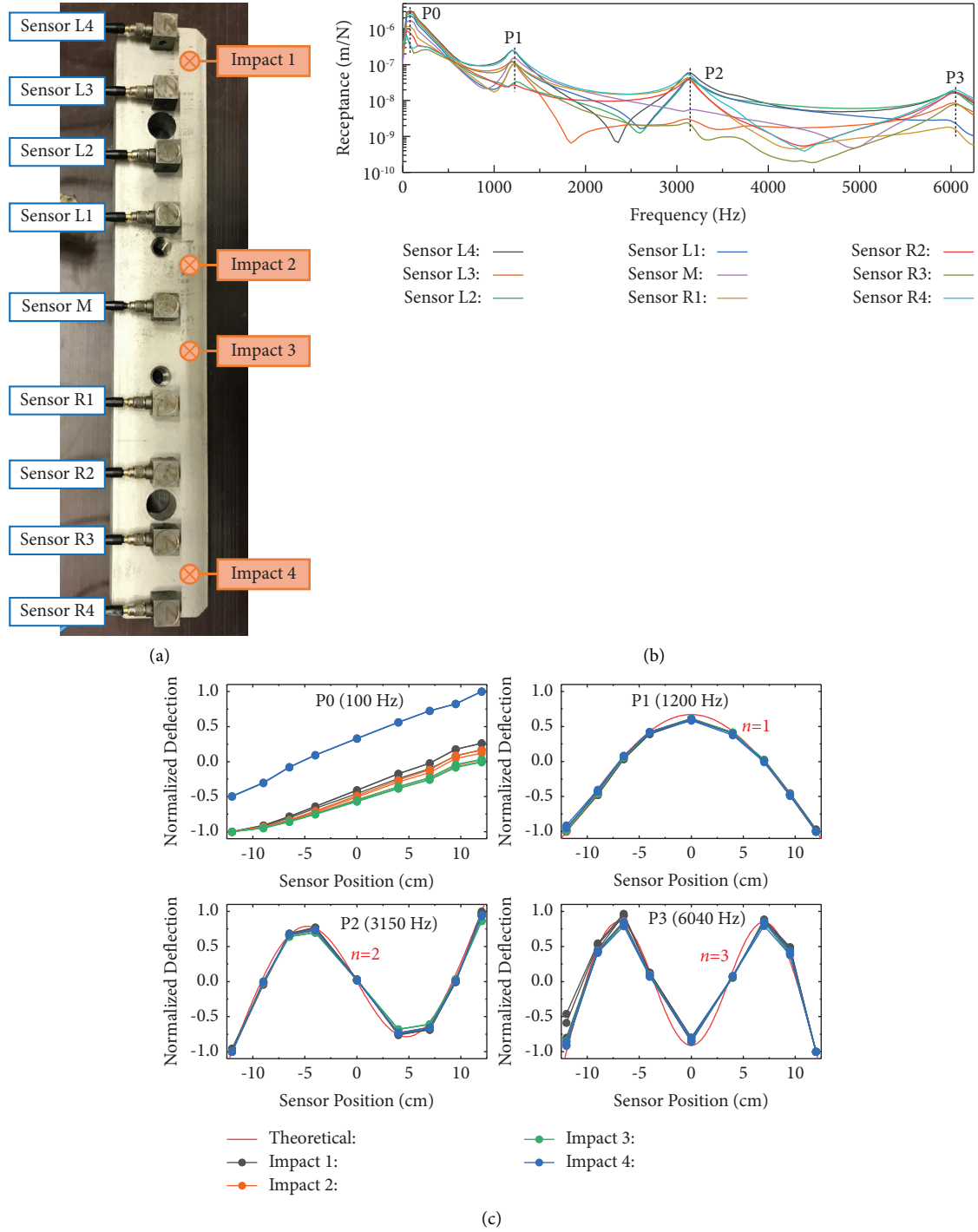
FIGURE 8: EMA and theoretical analysis of a free sleeper: (a) test setup; (b) FRFs of all sensors for impact 2; (c) mode shapes and frequencies of the four resonance peaks.

frequencies, are smooth, which is consistent with the finding in Section 4.3. The average frequency and mode shapes for each resonance peak are shown in Table 3, where the identified mode shapes deviate for different hammers and impact locations.

5.3. Comparisons between TFOMA and EMA. Moreover, we compute the theoretical mode shapes of a free-free beam of length 2.5 m according to (16) and (17). Furthermore, in Table 3, we match the identified modes of TFOMA with those of EMA and theoretical analysis while referring to the

(a)

(b)

(c)
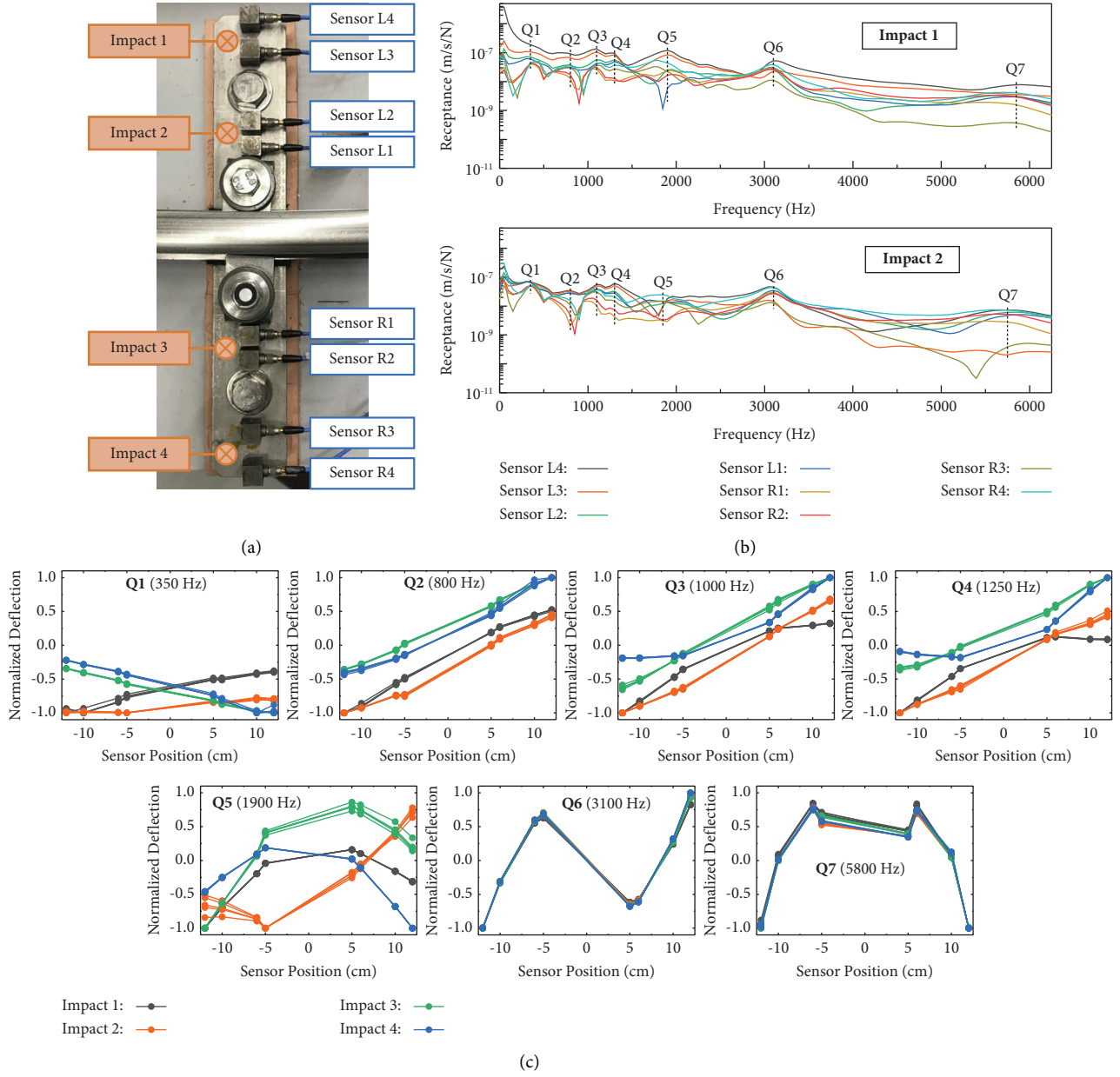
Figure 9: EMA results of the *in situ* sleeper in laboratory tests: (a) test setup; (b) FRFs of all sensors for impact 1 and 2; (c) mode shapes and frequencies of the seven resonance peaks.
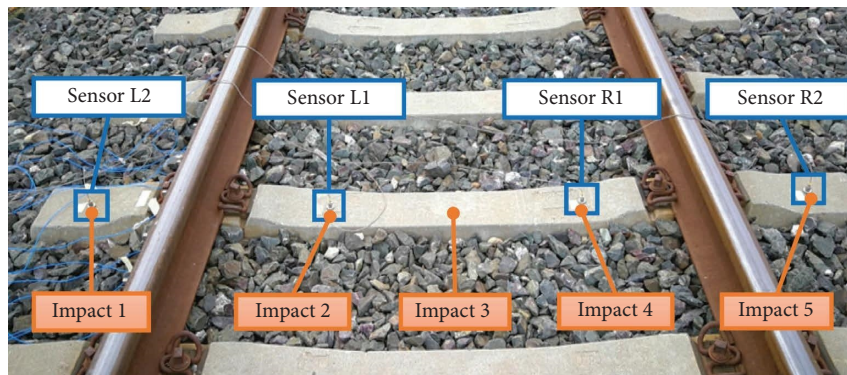
Figure 10: The instrumented sleeper in field tests.

TABLE 2: Selected parameters for field tests.

Number of segment n_c	Segment length n_b	Overlap ratio in PSD estimation α_b	Overlap ratio in STFDD α_s	Half kernel size in time a
1	5120 (0.2 s)	0.5	0.95	10
Half kernel size in frequency b	Contribution exponent of singular value λ_v	Contribution exponent of LMSS λ_l	Time resolution Δt	Frequency resolution Δf
5	1	3	10 ms	5 Hz
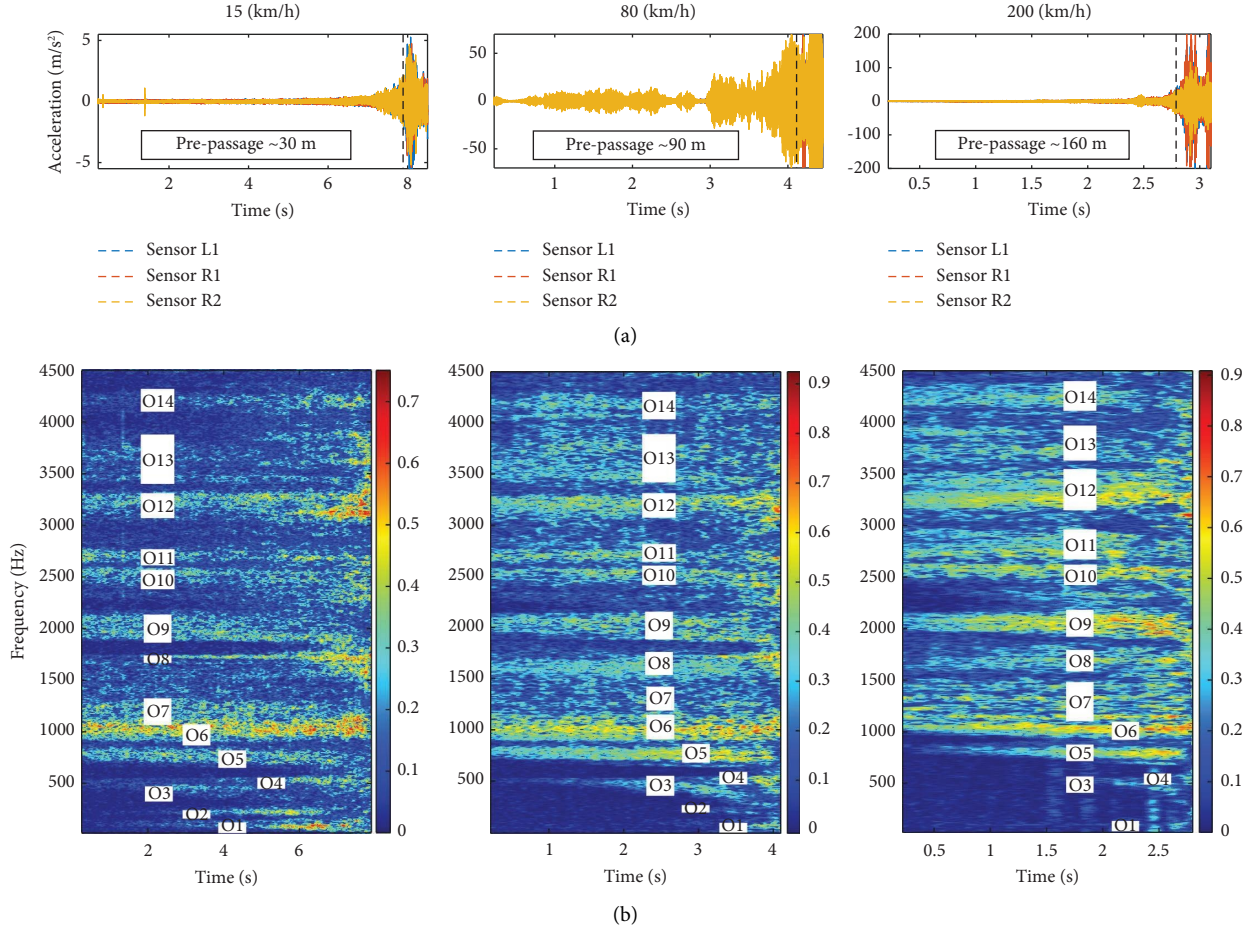
FIGURE 11: TFOMA results of field tests: (a) sleeper accelerations at 15 km/h, 80 km/h, and 200 km/h in the time domain; (b) MI spectrograms at 15 km/h, 80 km/h, and 200 km/h.

characteristics of sleeper modes reported in [35, 57]. The average *MAC* in Table 3 quantifies the consistency of mode shapes between TFOMA and EMA. The main findings are summarized below:

(i) TFOMA identifies the rigid-body motions of the sleeper at frequencies lower than those of the bending modes, which is consistent with [35, 57]. The bounce motion is more pronounced, which is consistent with the laboratory test. The rigid-body motions are not observed in EMA because the impact forces cannot effectively excite such modes.

(ii) In terms of mode shapes, both TFOMA and EMA consistently (with high *MAC* values) identify the 1st, 2nd, 4th, 5th, 7th, 8th, and 10th bending modes. However, neither identifies the 3rd, 6th, and 9th bending modes, probably because these modes are less dominant or the sensors are close to the nodes.

(iii) The frequencies of $E1$, $E2$, and $E4$ are close to those reported in [35, 57] under unloaded conditions. For the 1st and 2nd bending, the frequencies of TFOMA deviate from those of EMA, reflecting the influence of the train load. For high-order modes, the frequencies of TFOMA and EMA are very close.

(iv) Both TFOMA and EMA identify extra modes probably related to other components.

Furthermore, the pros and cons of TFOMA and EMA are discussed as follows:

(i) TFOMA can capture the change of modal characteristics over time and frequency, whereas EMA cannot.

(ii) TFOMA works under operational loads in a broad frequency range, but the excitation spectrum is usually not flat, which can cause errors in modal identification. EMA works under controlled excitations but requires manual impacts and also different hammers for different frequency ranges.

(iii) For a complex coupled system (e.g., a train-track system), the response of a component (e.g., a sleeper) depends not only on its own modal characteristics but also on the dynamical influence of other components (e.g., trains, rails, fasteners, and ballast). As a consequence, extra modes can be more pronounced in OMA than in EMA.

(iv) For each mode, the mode shapes identified by TFOMA spread within a certain variance, while

TABLE 3: Comparisons between the results of TFOMA, EMA, and theoretical analysis.
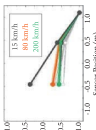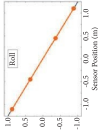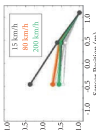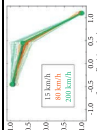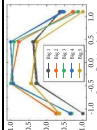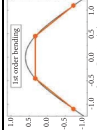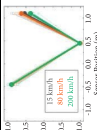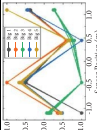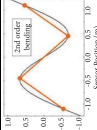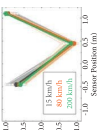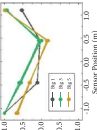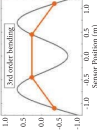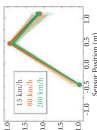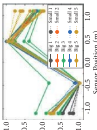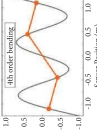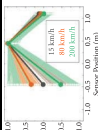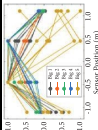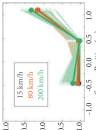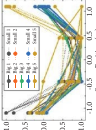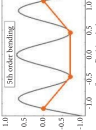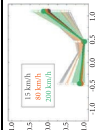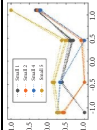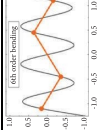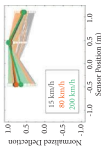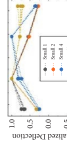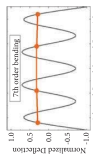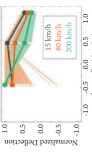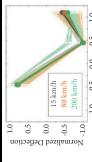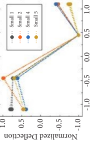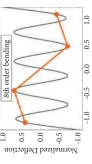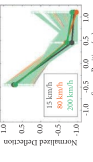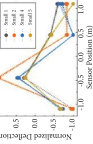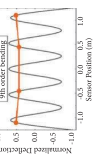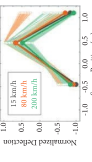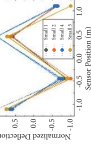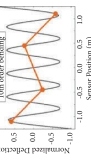
	TFOMA			EMA				Theoretical analysis		Comparisons
Order	Characteristics	Avg. freq	Mode shapes	Order	Avg. freq	Mode shapes	Avg. MAC	Order	Mode shape	
O1	They are pronounced when the train is close, especially at low speeds	$f_{15}=100\,\text{Hz}$ $f_{80}=95\,\text{Hz}$ $f_{200}=95\,\text{Hz}$		—	—	—	—	Bounce		TFOMA identifies the rigid-body motions, whereas EMA fails
O2		$f_{15}=235\,\text{Hz}$ $f_{80}=220\,\text{Hz}$		—	—	—	—	Roll		
O3	Its frequency drops as the train approaches	$f_{15}=475\,\text{Hz}$ $f_{80}=490\,\text{Hz}$ $f_{200}=495\,\text{Hz}$		E1	160 Hz		0.98	1st bending		TFOMA and EMA identify the 1st bending mode, while their frequencies deviate significantly
O4	It is pronounced when the train is close, especially at low speeds	$f_{15}=535\,\text{Hz}$ $f_{80}=540\,\text{Hz}$ $f_{200}=525\,\text{Hz}$		E2	395 Hz		0.97	2nd bending		TFOMA and EMA identify the 2nd bending mode, while their frequencies deviate
O5	Its frequency drops slightly	$f_{15}=760\,\text{Hz}$ $f_{80}=790\,\text{Hz}$ $f_{200}=800\,\text{Hz}$		E3	650 Hz		0.64	3rd bending		Neither TFOMA nor EMA identifies the 3rd bending mode
O6	It is the most dominant band at 15 km/h and 80 km/h	$f_{15}=1060\,\text{Hz}$ $f_{80}=1050\,\text{Hz}$ $f_{200}=1060\,\text{Hz}$		E4	975 Hz (big); 1000 Hz (small)		0.99	4th bending		TFOMA and EMA identify the 4th bending mode, while their frequencies are consistent
O7	Its frequency band is wide while without clear boundaries	$f_{15}=1230\,\text{Hz}$ $f_{80}=1270\,\text{Hz}$ $f_{200}=1280\,\text{Hz}$		E5	1250 Hz		0.34	—	—	TFOMA and EMA identify extra modes
O8	Its frequency band is narrow at 15 km/h and wider at higher speeds	$f_{15}=1725\,\text{Hz}$ $f_{80}=1695\,\text{Hz}$ $f_{200}=1705\,\text{Hz}$		E6	1700 Hz (big); 1700 Hz (small)		0.99	5th bending		TFOMA and EMA identify the 5th bending mode, while their frequencies are consistent
O9	It is more pronounced at higher speeds. Its frequency drops slightly	$f_{15}=1995\,\text{Hz}$ $f_{80}=2050\,\text{Hz}$ $f_{200}=2060\,\text{Hz}$		E7	2100 Hz		0.82	6th bending		Neither TFOMA nor EMA identifies the 6th bending mode.

TABLE 3: Continued.

	TFOMA				EMA				Theoretical analysis		Comparisons
Order	Characteristics	Avg. freq	Mode shapes	Order	Avg. freq	Mode shapes	Avg. MAC	Order	Mode shape	
O10	They are more pronounced at higher speeds	$f_{15} = 2520$ Hz $f_{80} = 2530$ Hz $f_{200} = 2580$ Hz		E8	2620 Hz		0.93	7th bending		TFOMA and EMA identify the 7th bending mode, while their frequencies are consistent.
O11		$f_{15} = 2695$ Hz $f_{80} = 2700$ Hz $f_{200} = 2710$ Hz					0.99			
O12	Its frequency increases slightly as the train approaches	$f_{15} = 3220$ Hz $f_{80} = 3240$ Hz $f_{200} = 3230$ Hz		E9	3200 Hz		0.99	8th bending		TFOMA and EMA identify the 8th bending mode, while their frequencies are consistent.
O13	Its frequency band is wide while without clear boundaries	$f_{15} = 3645$ Hz $f_{80} = 3725$ Hz $f_{200} = 3710$ Hz		E10	3720 Hz		0.99	9th bending		Neither TFOMA nor EMA identifies the 9th bending mode, while their mode shapes are similar.
O14	It is more pronounced at higher speeds	$f_{15} = 4180$ Hz $f_{80} = 4190$ Hz $f_{200} = 4210$ Hz		E11	4160 Hz		0.98	10th bending		TFOMA and EMA identify the 10th bending mode, while their frequencies are consistent.

(a)

(b)

(c)

(d)

(e)
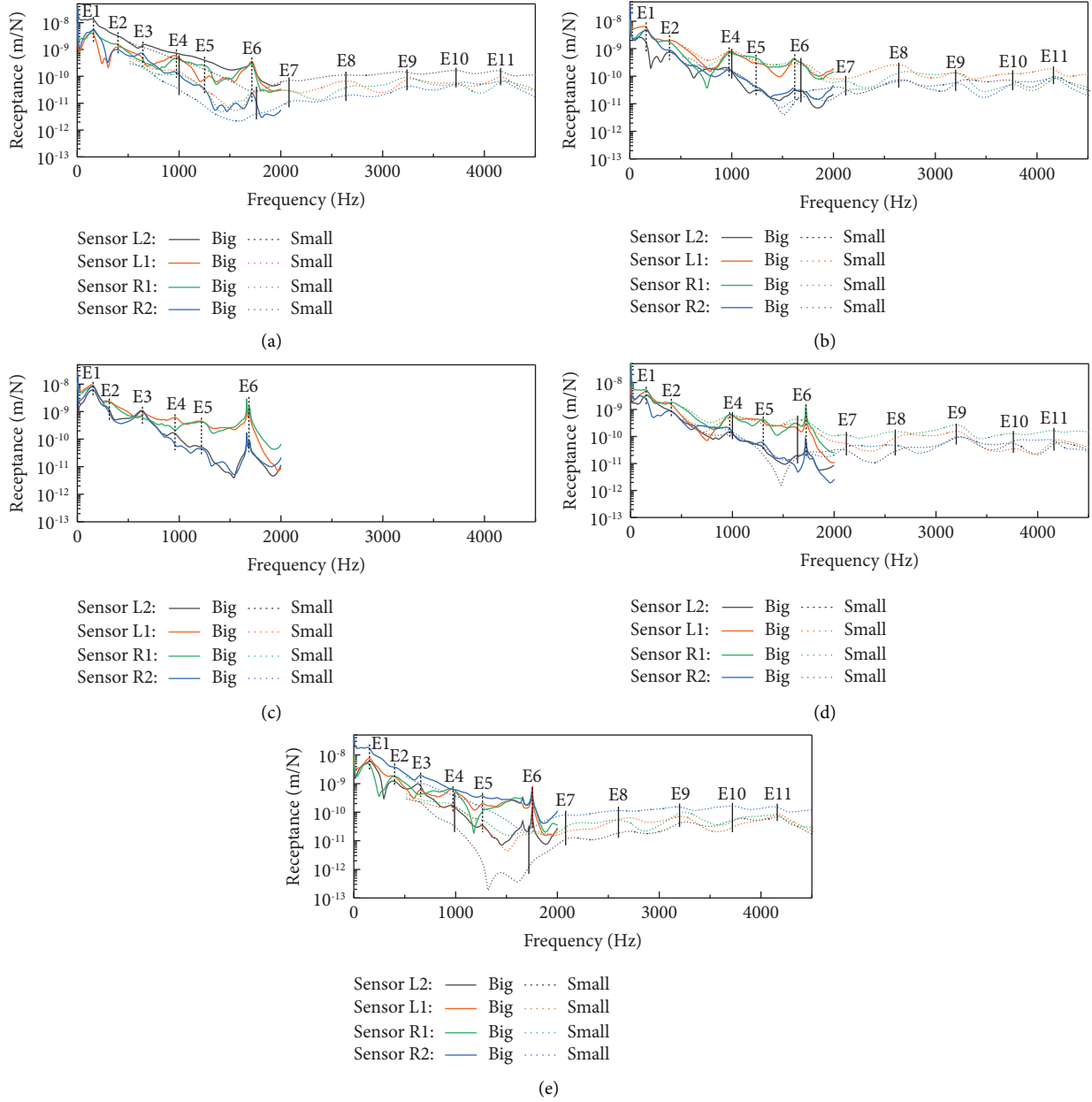
FIGURE 12: EMA results of field tests: (a) FRFs for impact 1; (b) FRFs for Impact 2; (c) FRFs for Impact 3; (d) FRFs for Impact 4; (e) FRFs for impact 5.

those identified by EMA are sensitive to impact locations and may disappear or be distorted when the impact is close to a node or an edge.

(v) TFOMA can provide informative results from acceleration measurements of only a few seconds under operational conditions, whereas EMA requires longer experimental time, more workload, and temporary operation shutdowns.

6. Discussion

6.1. Estimation of Damping Ratios. This paper mainly focuses on estimating damped natural frequencies and mode shapes. In this section, the estimation of damping ratios is discussed. First, for the *in situ* sleeper in the laboratory tests, the damping ratio of each peak band is obtained while estimating the natural frequencies in Section 4.1. Besides, we estimate the damping ratios from the FRFs in Section 4.3
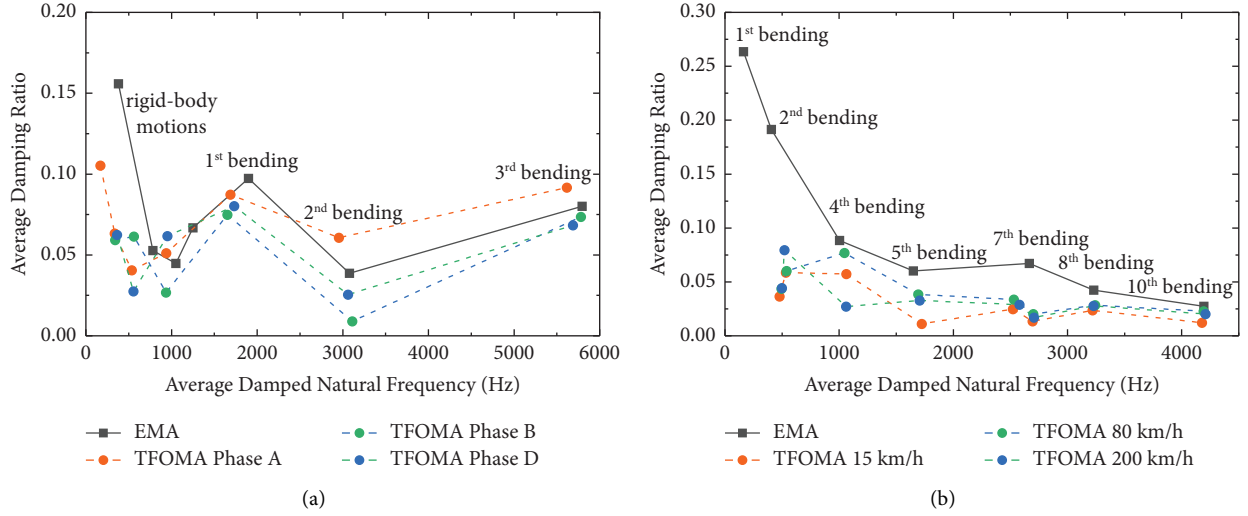
FIGURE 13: Comparison of damping ratio estimation between TFOMA and EMA: (a) laboratory tests; (b) field tests.

using the traditional peak-picking method [58]. Then, for all the matched modes in Section 4.4, the estimated damping ratios are plotted against their natural frequencies in Figure 13(a). For most modes, TFOMA in different phases produces damping ratio estimates similar to EMA while underestimating those at low frequencies.

Similarly, the damping ratios of the sleeper in the field tests are estimated and plotted in Figure 13(b). The results of TFOMA are similar at different speeds, but the estimated damping ratios are lower than those of EMA. These deviations may come from two sources. On the one hand, the different loading conditions can lead to different modal characteristics, including damping ratios. This effect is pronounced for railway tracks since the train load is enormous. On the other hand, the estimation based on a truncated spectrum (either in TFOMA or EMA) can cause errors, especially when the frequency resolution is low or adjacent modes affect each other [21, 23]. In summary, TFOMA can provide accurate damping estimates in the case of well-separated modes, but it needs further improvement to handle structures with significant nonlinearity and dense modes.

6.2. Identification of Closely Spaced Modes.
In this paper, the proposed method is applied to the modal identification of railway sleepers, where the bending modes of different orders are separated. It has the potential to identify closely spaced modes by involving multiple nonzero singular values. This section aims to demonstrate such capability using a simulation example. As shown in Figure 14(a), a rectangular plate suspended by springs and dampers vibrates in the x-y plane with three degrees of freedom $-x$, y, and θ. External excitation forces are applied at the upper right corner, and the equations of motion are given as follows:

$$\begin{cases} m\ddot{x} + 2k_x x + 2c_x \dot{x} = P_x, \\ m\ddot{y} + 2k_y y + 2c_y \dot{y} = P_y, \\ I\ddot{\theta} + 2bk_x\theta + 2ak_y\theta + 2bc_x\dot{\theta} + 2ac_y\dot{\theta} = aP_y - bP_x. \end{cases}$$
(18)

Based on the parameters and excitations defined in Table 4, (18) is solved numerically using the Newmark-beta method [59] with a time step of 0.2 ms. The bidirectional accelerations of the four edge centers are fed into the TFOMA method with the parameters in Table 5. The number of segment $n_c = 2$ is used to distinguish the two translational modes, which are closely spaced since they have equal natural frequencies due to equal stiffness.

Two MI spectrograms are obtained, as shown in Figures 14(b)–14(c), with eight peak bands (with $MI > 0.8$) identified in different phases of the response. The estimated natural frequencies and mode shapes are shown in Figure 14(d). In 0~2 s, the translational mode in the x direction is identified ($X1$), whereas the one in the y direction is not identified since the excitation is applied only in the x direction. When the excitation is applied only in the y direction in 2~4 s, the translational mode in the y direction is identified ($Y1$), while the one in the x direction is still identifiable from the decay response ($Y3$). When the excitations are applied in both directions, the two translational modes are identified ($XY1$ and $XY3$), and $XY1$ (in the 1st spectrogram) is more dominant than $XY3$ (in the 2nd spectrogram) since the excitation in the y direction has greater power. Moreover, the rotational mode is identified in all three phases ($X2$, $Y2$, and $XY2$). For all modes, the estimated frequencies are consistent with the engine frequencies calculated from the model parameters. The simulation result demonstrates that the proposed method

(a)

(b)

(c)

(d)
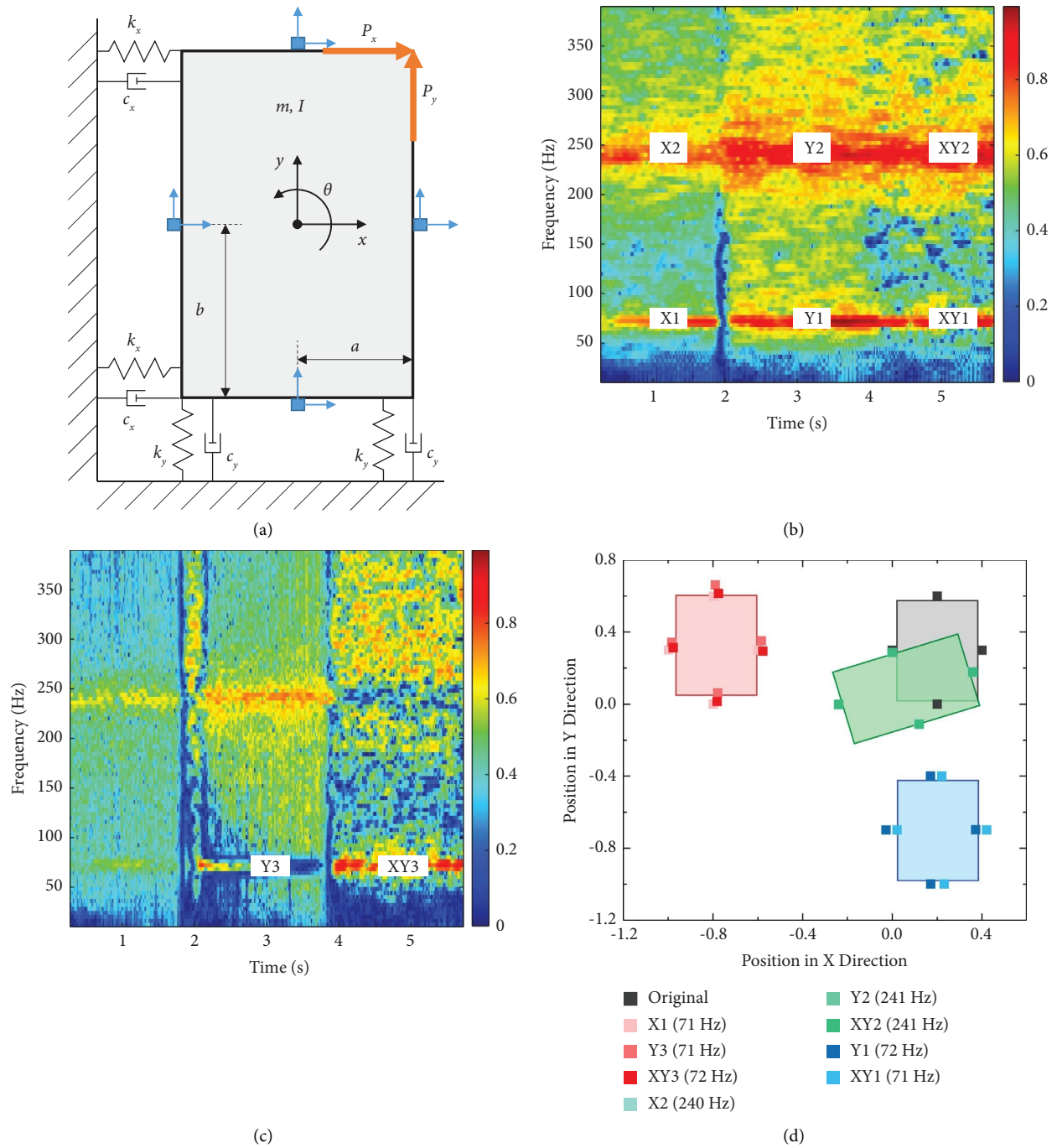
Figure 14: TFOMA results of a vibrating plate: (a) plate model; (b) 1st MI spectrogram; (c) 2nd MI spectrogram; (d) natural frequencies and mode shapes of different peak bands.

TABLE 4: Parameters and excitations of the plate.

Mass m	Half width a	Half height b	Moment of inertia I	Stiffness k_x, k_y	Damping c_x, c_y
1 kg	0.2 m	0.3 m	$m(a^2+b^2)/3$	100 kN/m	2 N s/m
Excitation P_x (0~2 s)	Excitation P_y (0~2 s)	Excitation P_x (2~4 s)	Excitation P_y (2~4 s)	Excitation P_x (4~6 s)	Excitation P_y (4~6 s)
White noise with the power of 10 dBW	0	0	White noise with the power of 20 dBW	White noise with the power of 10 dBW	White noise with the power of 20 dBW

TABLE 5: Selected parameters for the plate.

Number of segment n_c	Segment length n_b	Overlap ratio in PSD estimation α_b	Overlap ratio in STFDD α_s	Half kernel size in time a
2	1250 (0.25 s)	0.5	0.95	5
Half kernel size in frequency b	Contribution exponent of singular value λ_v	Contribution exponent of LMSS λ_l	Time resolution Δt	Frequency resolution Δf
3	1	3	18.75 ms	4 Hz

can distinguish closely spaced modes under nonstationary excitations as long as the modes are effectively excited. We expect the validity of this capability to hold in real-world scenarios, while it remains to be demonstrated.

7. Conclusions

This paper presents an interpretable OMA method in time-frequency representation. Short-time FDD and a convolution-based strategy are proposed to obtain singular values and local mode shape similarity, respectively, which are further fused into mode indicators by a fuzzy-based strategy. TFOMA is an explicit tool that provides a global view of modal characteristics and estimates of modal parameters. It is applicable to strongly nonstationary responses under time-varying loads and conditions and is robust to the length of signals due to its discrete and localized nature. Its interpretability is enhanced by including physical information from the user's prior knowledge in selecting parameters and peak bands.

In this paper, TFOMA identifies the rigid-body motions and bending modes of the sleepers at frequencies up to 6,500 Hz in the laboratory tests and 4,500 Hz in the field tests. The passage response provides similar results to the impact response, while the prepassage phase slightly outperforms the postpassage phase. TFOMA works effectively at speeds up to 200 km/h by using only three sensors, and some high-frequency modes are identifiable when the train is 150 m away. TFOMA provides identification results comparable to EMA, while their deviations reflect the dynamical influence of train loading and other track components.

In future research, theoretical analyses and numerical simulations will be carried out to investigate the characteristics of train loads on tracks and decouple the dynamics of different components in a train-track system. Meanwhile, the proposed method will be further improved to provide adaptive time and frequency resolutions (especially for signals with significant nonstationarity or nonuniform frequency bands) and to more accurately estimate damping ratios for nonlinear structures with dense modes. Moreover, the uncertainty of modal analysis will be quantified so as to assess the confidence level of identification results.

Data Availability

The data used to support the findings of this study are available from the corresponding author upon reasonable request.

Conflicts of Interest

The authors declare that there are no conflicts of interest regarding the publication of this article.

Acknowledgments

References

[1] B. Peeters and G. De Roeck, "Stochastic system identification for operational modal analysis: a review," *Journal of Dynamic Systems, Measurement, and Control*, vol. 123, no. 4, pp. 659–667, 2001.

[2] C. Rainieri and G. Fabbrocino, *Operational Modal Analysis of Civil Engineering Structures*, Springer, New York, NY, USA, 2014.

[3] F. B. Zahid, Z. C. Ong, and S. Y. Khoo, "A review of operational modal analysis techniques for in-service modal identification," *Journal of the Brazilian Society of Mechanical Sciences*, vol. 42, no. 8, pp. 1–18, 2020.

[4] K. V. Yuen and L. S. Katafygiotis, "Bayesian time–domain approach for modal updating using ambient data," *Probabilistic Engineering Mechanics*, vol. 16, no. 3, pp. 219–231, 2001.

[5] P. Guillaume, P. Verboven, and S. Vanlanduit, "Frequency-domain maximum likelihood identification of modal parameters with confidence intervals," in *Proceedings of the International Seminar on Modal Analysis*, vol. 1, pp. 359–366, Katholieke Universiteit Leuven, 1998.

[6] J. Javh, J. Slavič, and M. Boltežar, "High frequency modal identification on noisy high-speed camera data," *Mechanical Systems and Signal Processing*, vol. 98, pp. 344–351, 2018.

[7] S. K. Au, F. L. Zhang, and Y. C. Ni, "Bayesian operational modal analysis: theory, computation, practice," *Computers & Structures*, vol. 126, pp. 3–14, 2013.

[8] W. J. Yan and L. S. Katafygiotis, "A two-stage fast Bayesian spectral density approach for ambient modal analysis. Part I: posterior most probable value and uncertainty," *Mechanical Systems and Signal Processing*, vol. 54, pp. 139–155, 2015.

[9] S. K. Au, "Fast Bayesian FFT method for ambient modal identification with separated modes," *Journal of Engineering Mechanics*, vol. 137, no. 3, pp. 214–226, 2011.

[10] H. F. Lam, J. Hu, and J. H. Yang, "Bayesian operational modal analysis and Markov chain Monte Carlo-based model updating of a factory building," *Engineering Structures*, vol. 132, pp. 314–336, 2017.

[11] B. Li and S. K. Au, "An expectation-maximization algorithm for Bayesian operational modal analysis with multiple (possibly close) modes," *Mechanical Systems and Signal Processing*, vol. 132, pp. 490–511, 2019.

[12] S. K. Au, "Fast Bayesian ambient modal identification in the frequency domain, Part I: posterior most probable value," *Mechanical Systems and Signal Processing*, vol. 26, pp. 60–75, 2012.

[13] C. Y. Shih, Y. G. Tsuei, R. J. Allemang, and D. L. Brown, "Complex mode indication function and its applications to spatial domain parameter estimation," *Mechanical Systems and Signal Processing*, vol. 2, no. 4, pp. 367–377, 1988.

[14] R. Brincker, L. Zhang, and P. Andersen, "Modal identification of output-only systems using frequency domain decomposition," *Smart Materials and Structures*, vol. 10, no. 3, pp. 441–445, 2001.

[15] A. Elhattab, N. Uddin, and E. Obrien, "Identifying localized bridge damage using frequency domain decomposition," *Proceedings of the 26th ASNT Research Symposium*, pp. 75–83, 2017.

[16] M. M. Alamdari, A. Anaissi, N. L. D. Khoa, and S. Mustapha, "Frequency domain decomposition-based multisensor data fusion for assessment of progressive damage in structures," *Structural Control and Health Monitoring*, vol. 26, no. 2, pp. 1–19, 2019.

[17] A. Fernández-Navamuel, D. Zamora-Sánchez, T. Varona-Poncela et al., "Vibration-based SHM strategy for a real time alert system with damage location and quantification," in *European Workshop on Structural Health Monitoring*, pp. 245–255, Springer Cham, Berlin, Germany, 2020.

[18] E. J. Obrien and A. Malekjafarian, "A mode shape-based damage detection approach using laser measurement from a vehicle crossing a simply supported bridge," *Structural Control and Health Monitoring*, vol. 23, no. 10, pp. 1273–1286, 2016.

[19] S. T. Lin, Y. Lu, M. M. Alamdari, and N. L. Khoa, "Field test investigations for condition monitoring of a concrete culvert bridge using vibration responses," *Structural Control and Health Monitoring*, vol. 27, no. 10, Article ID e2614, 2020.

[20] R. Brincker, C. E. Ventura, and P. Andersen, "Damping estimation by frequency domain decomposition," in *Proceedings of the IMAC 19: A Conference on Structural Dynamics: februar 5-8, 2001*, pp. 698–703, Society for Experimental Mechanics, Kissimmee, FL, USA, February 2001.

[21] P. T. Brewick and A. W. Smyth, "An investigation of the effects of traffic induced local dynamics on global damping estimates using operational modal analysis," *Mechanical Systems and Signal Processing*, vol. 41, no. 1-2, pp. 433–453, 2013.

[22] T. Wang, L. Zhang, and Y. Tamura, "An operational modal analysis method in frequency and spatial domain," *Earthquake Engineering and Engineering Vibration*, vol. 4, no. 2, pp. 295–300, 2005.

[23] L. Zhang, T. Wang, and Y. Tamura, "A frequency–spatial domain decomposition (FSDD) method for operational modal analysis," *Mechanical Systems and Signal Processing*, vol. 24, no. 5, pp. 1227–1239, 2010.

[24] F. Pioldi, R. Ferrari, and E. Rizzi, "Output-only modal dynamic identification of frames by a refined FDD algorithm at seismic input and high damping," *Mechanical Systems and Signal Processing*, vol. 68-69, pp. 265–291, 2016.

[25] F. Pioldi, R. Ferrari, and E. Rizzi, "Earthquake structural modal estimates of multi-storey frames by a refined Frequency Domain Decomposition algorithm," *Journal of Vibration and Control*, vol. 23, no. 13, pp. 2037–2063, 2017.

[26] Ç. Hızal, "Modified frequency and spatial domain decomposition method based on maximum likelihood estimation," *Engineering Structures*, vol. 224, Article ID 111007, 2020.

[27] S. F. Ghahari, F. Abazarsa, M. A. Ghannad, M. Celebi, and E. Taciroglu, "Blind modal identification of structures from spatially sparse seismic response signals," *Structural Control and Health Monitoring*, vol. 21, no. 5, pp. 649–674, 2014.

[28] X. J. Yao, T. H. Yi, C. Qu, and H. N. Li, "Blind modal identification using limited sensors through modified sparse component analysis by time-frequency method," *Computer-Aided Civil and Infrastructure Engineering*, vol. 33, no. 9, pp. 769–782, 2018.

[29] J. Lardies and S. Gouttebroze, "Identification of modal parameters using the wavelet transform," *International Journal of Mechanical Sciences*, vol. 44, no. 11, pp. 2263–2283, 2002.

[30] T. P. Le and P. Argoul, "Continuous wavelet transform for modal identification using free decay response," *Journal of Sound and Vibration*, vol. 277, no. 1-2, pp. 73–100, 2004.

[31] M. Ülker-Kaustell and R. Karoumi, "Application of the continuous wavelet transform on the free vibrations of a steel–concrete composite railway bridge," *Engineering Structures*, vol. 33, no. 3, pp. 911–919, 2011.

[32] T. P. Le and P. Paultre, "Modal identification based on continuous wavelet transform and ambient excitation tests," *Journal of Sound and Vibration*, vol. 331, no. 9, pp. 2023–2037, 2012.

[33] T. P. Le and P. Paultre, "Modal identification based on the time–frequency domain decomposition of unknown-input dynamic tests," *International Journal of Mechanical Sciences*, vol. 71, pp. 41–50, 2013.

[34] T. P. Le and P. Argoul, "Distinction between harmonic and structural components in ambient excitation tests using the time–frequency domain decomposition technique," *Mechanical Systems and Signal Processing*, vol. 52, pp. 29–45, 2015.

[35] H. F. Lam, M. T. Wong, and Y. B. Yang, "A feasibility study on railway ballast damage detection utilizing measured vibration of in situ concrete sleeper," *Engineering Structures*, vol. 45, pp. 284–298, 2012.

[36] M. Oregui, Z. Li, and R. Dollevoet, "Identification of characteristic frequencies of damaged railway tracks using field hammer test measurements," *Mechanical Systems and Signal Processing*, vol. 54, pp. 224–242, 2015.

[37] R. Janeliukstis, A. Clark, S. Rucevskis, and S. Kaewunruen, "Vibration-based damage identification in railway concrete sleepers," in *Proceedings of the The 4th Conference on Smart Monitoring, Assessment and Rehabilitation of Civil Structures*, pp. 1–9, Zurich, Switzerland, April 2017.

[38] C. Shen, Z. Li, and R. Dollovoet, "A novel method for railway crossing monitoring based on ambient vibration caused by train-track interaction," in *Proceedings of the IAVSD International Symposium on Dynamics of Vehicles on Roads and Tracks*, pp. 133–141, Vienna, Austria, August 2019.

[39] T. X. Wu and D. J. Thompson, "The effects of track non-linearity on wheel/rail impact," *Proceedings of the Institution of Mechanical Engineers, Part F: Journal of Rail and Rapid Transit*, vol. 218, no. 1, pp. 1–15, 2004.

[40] M. Oregui, A. De Man, M. F. Woldekidan, Z. Li, and R. Dollovoet, "Obtaining railpad properties via dynamic mechanical analysis," *Journal of Sound and Vibration*, vol. 363, pp. 460–472, 2016.

[41] J. Sadeghi, M. Seyedkazemi, and A. Khajehdezfuly, "Nonlinear simulation of vertical behavior of railway fastening system," *Engineering Structures*, vol. 209, Article ID 110340, 2020.

[42] P. Welch, "The use of fast Fourier transform for the estimation of power spectra: a method based on time averaging over short, modified periodograms," *IEEE Transactions on Audio and Electroacoustics*, vol. 15, no. 2, pp. 70–73, 1967.

[43] Ç. Hızal and E. Aktaş, "Probabilistic investigation of error propagation in frequency domain decomposition-based operational modal analysis," *Structural Control and Health Monitoring*, vol. 28, no. 8, Article ID e2759, 2021.

[44] N. Kehtarnavaz, *Digital Signal Processing System Design*, Academic Press, 2 edition, 2008.

[45] A. Buades, B. Coll, and J. M. Morel, "A review of image denoising algorithms, with a new one," *Multiscale Modeling and Simulation*, vol. 4, no. 2, pp. 490–530, 2005.

[46] L. Fan, F. Zhang, H. Fan, and C. Zhang, "Brief review of image denoising techniques," *Visual Computing for Industry, Biomedicine, and Art*, vol. 2, no. 1, pp. 1–12, 2019.

[47] P. Getreuer, "A survey of Gaussian convolution algorithms," *Image Processing On Line*, pp. 286–310, 2013.

[48] W. K. Ling, *Nonlinear Digital Filters: Analysis and Applications*, Academic Press, 2010.

[49] H. Singh, J. Raj, G. Kaur, and T. Meitzler, "Image fusion using fuzzy logic and applications," *IEEE International Conference on Fuzzy Systems*, vol. 1, pp. 337–340, 2004.

[50] M. Zhu and Y. Yang, "A new image fusion algorithm based on fuzzy logic," *International Conference on Intelligent Computation Technology and Automation*, vol. 2, pp. 83–86, 2008.

[51] P. Balasubramaniam and V. P. Ananthi, "Image fusion using intuitionistic fuzzy sets," *Information Fusion*, vol. 20, pp. 21–30, 2014.

[52] M. Naeimi, Z. Li, R. H. Petrov, J. Sietsma, and R. Dollevoet, "Development of a new downscale setup for wheel-rail contact experiments under impact loading conditions," *Experimental Techniques*, vol. 42, no. 1, pp. 1–17, 2018.

[53] W. A. Fladung, "Windows used for impact testing," in *Proceedings-SPIE the International Society for Optical Engineering*, pp. 1662–1666, SPIE International Society for Optical, 1997.

[54] P. Zhang, S. Li, A. Núñez, and Z. Li, "Multimodal dispersive waves in a free rail: numerical modeling and experimental investigation," *Mechanical Systems and Signal Processing*, vol. 150, Article ID 107305, 2021.

[55] S. S. Rao, *Mechanical Vibrations*, Pearson, USA, 5 edition, 2011.

[56] C. Shen, R. Dollevoet, and Z. Li, "Fast and robust identification of railway track stiffness from simple field measurement," *Mechanical Systems and Signal Processing*, vol. 152, Article ID 107431, 2021.

[57] S. Kaewunruen and A. M. Remennikov, "Sensitivity analysis of free vibration characteristics of an in situ railway concrete sleeper to variations of rail pad parameters," *Journal of Sound and Vibration*, vol. 298, no. 1-2, pp. 453–461, 2006.

[58] R. J. Allemang and L. B. David, "Experimental modal analysis and dynamic component synthesis," *Modal Parameter Estimation*, Flight Dynamics Laboratory, 1987.

[59] N. M. Newmark, "A method of computation for structural dynamics," *Journal of the Engineering Mechanics Division*, vol. 85, no. 3, pp. 67–94, 1959.